Renewable Energy 185 (2022) 1167–1176

Contents lists available at ScienceDirect

Renewable Energy

journal homepage: www.elsevier.com/locate/renene

Optimisation of high-performance, cobalt-free $SrFe_{1-x}Mo_xO_{3-\delta}$ cathodes for solid oxide fuel cells prepared by spray pyrolysis

Víctor Zapata-Ramírez [a], Paula Rosendo-Santos [b], Ulises Amador [b], Clemens Ritter [c], Glenn C. Mather [a], Domingo Pérez-Coll [a, *]

[a] Instituto de Cerámica y Vidrio, CSIC, Campus de Cantoblanco, 28049, Madrid, Spain
[b] Universidad San Pablo-CEU, CEU Universities, Facultad de Farmacia, Departamento de Química y Bioquímica, Urbanización Monteprincipe, Boadilla del Monte, E-28668, Madrid, Spain
[c] Institut Laue-Langevin, BP 156-38042, Grenoble, Cedex 9, France

ARTICLE INFO

Article history:
Received 16 July 2021
Received in revised form
8 December 2021
Accepted 23 December 2021
Available online 31 December 2021

Keywords:
SOFC
Cobalt-free air electrode
Spray pyrolysis
Electrochemical stability
Fuel-cell performance

ABSTRACT

Strontium-ferrite-based perovskites as cobalt-free cathodes for intermediate-temperature solid oxide fuel cells (IT-SOFCs) have been analysed employing structural, stability and electrochemical studies. Neutron diffraction of $SrFeO_{3-\delta}$ and $SrFe_{0.9}Mo_{0.1}O_{3-\delta}$ prepared by a Pechini method confirmed that $SrFeO_{3-\delta}$ undergoes a phase transition from tetragonal to cubic symmetry at 300–400 °C, whereas Mo-doping stabilises cubic symmetry in the range RT-900 °C. Spray-pyrolysed electrodes offered significantly lower area-specific resistances of 0.2 and 0.11 Ω cm^2 for $SrFeO_{3-\delta}$ and $SrFe_{0.9}Mo_{0.1}O_{3-\delta}$ at 700 °C, respectively, in comparison to their analogues synthesised by the Pechini method (0.55 and 0.42 Ω cm^2), and lower grain size, as confirmed by scanning electron microscopy. Thermal cycling and ageing studies indicated a more robust response for the spray-pyrolysed electrodes, in particular the Mo-doped phase, which achieved a stable electrode-polarisation resistance <0.1 Ω cm^2 for 10 heating/cooling cycles and 100 h of ageing at 700 °C. Anode-supported single cells with a thin $Ce_{0.9}Gd_{0.1}O_{2-\delta}$ electrolyte produced performances of 0.5 and 0.9 W cm^{-2} at 700 and 800 °C, respectively. $SrFe_{0.9}Mo_{0.1}O_{3-\delta}$ deposited by spray pyrolysis is, thus, proposed as a promising cobalt-free cathode for IT-SOFC based on its good structural stability and highly competitive electrochemical performance.

1. Introduction

One of the main goals of the United Nations Horizon 2030 action plan is to “ensure access to affordable, reliable, sustainable and modern energy for all” [1]. To achieve this, readily accessible clean energies are required on a global scale. Hydrogen as a fuel source, which is converted to electrical energy in fuel cells, is becoming an increasingly relevant alternative in this impending change in the way we use energy. There are several types of fuel cells, catalogued according to the nature of the electrolyte. One of the most prominent devices is the solid oxide fuel cell (SOFC), with a ceramic-based electrolyte, which affords highly competitive efficiencies, scalability through modularity, silent operation and pollution-free emissions [2–4].

Nevertheless, the high operation temperature of SOFCs imposes a requirement for expensive balance-of-plant materials and may result in excessive system degradation [2,5,6]. Reducing the operation temperature to the intermediate range (500–800 °C) would, thus, greatly enhance the viability of these devices in a series of applications. High performance IT-SOFCs (Intermediate temperature solid oxide fuel cells) commonly use perovskites ($ABO_{3-\delta}$) with mixed valence B cations for air electrodes as high electronic and ionic conductivity may be achieved in this temperature range [7]. Further enhancements may be gained through careful doping of the A or B cation positions [5,8–10], advanced processing techniques [11–16] or the adoption of active interlayers between the electrode and electrolyte [17–19].

Perovskites based on strontium cobaltite have large thermal expansion coefficients (TEC) but generally exhibit excellent electrochemical properties, and doped variants are widely studied with the goal of reducing TEC. However, the use of cobalt comes with numerous undesirable aspects, including inducement of respiratory problems in humans [20], environmental concerns surrounding its extraction [21], and a fluctuating price due to its location in unstable regions [22]. Hence, much effort is focused on reducing the cobalt content of IT-SOFC electrodes.

* Corresponding author.
E-mail address: dpcoll@icv.csic.es (D. Pérez-Coll).

https://doi.org/10.1016/j.renene.2021.12.121

Strontium ferrite-based materials are considered as potential alternatives to the cobaltites due to their lower cost and environmental impact, and higher stability; however, in many cases, they require a higher synthesis temperature (1200–1400 °C) to obtain monophasic material on doping with low contents of high-valence cations, such as zirconium, titanium, niobium, tungsten or antimonium [23–30]. It has been shown that phase purity can be achieved by different methods at similar temperatures to those used for strontium cobaltites (~1000 °C) on doping with 10 at.% molybdenum on the B position of $SrFeO_{3-\delta}$ [17,31]. Among different processing techniques employed to reduce the synthesis temperature, spray pyrolysis involves spraying the reaction precursors directly onto the substrate at high temperature (250–450 °C). This *in-situ* pre-treatment may improve the adherence and stability of the electrode-electrolyte interface.

Our previous work demonstrated the good performance of $SrFeO_{3-\delta}$ and $SrFe_{0.9}Mo_{0.1}O_{3-\delta}$ as air electrodes in both fuel-cell and electrolysis modes, with an especially competitive performance under anodic polarisation [31]. However, the working temperature leads to significant modifications of oxygen nonstoichiometry, with direct influence on the structural and electrochemical properties of $SrFeO_{3-\delta}$. A deeper investigation of the structural and stability of the system is therefore, warranted. Here, in addition to undertaking this study, we investigate spray-pyrolysis as a deposition method for improving electrochemical performance, which is analysed through both polarisation and single fuel-cell measurements.

2. Experimental

2.1. Synthesis

$SrFe_{1-x}Mo_xO_{3-\delta}$ powders (x = 0, 0.1; hereafter denoted as SFO-P and SFM-P) were synthesised with a citrate-nitrate process based on a modified Pechini method [32]. $Sr(NO_3)_2$, $Fe(NO_3)_3 \cdot xH_2O$ and $(NH_4)_6Mo_7O_{24} \cdot xH_2O$ were dissolved in distilled water with continuous stirring at 50 °C, with addition of citric acid (10:1 M ratio) and ethylene glycol (40:1 M ratio). The solution was slowly evaporated at 120 °C for 12 h and heated in air at 350 then 600 °C for 4 h at each temperature, to remove residual organic matter. Calcined materials were milled in an agate mortar, followed by a thermal treatment at 1000 °C for 10 h to obtain monophasic perovskite. The resulting material was then attrition milled at 400 rpm for 2 h in a Fritsch pulverisette 6 planetary ball mill.

Spray-pyrolysis was carried out using a Holmarc HO-TH-04BT instrument to synthesise and deposit thin-film layers of $SrFeO_{3-\delta}$ and $SrFe_{0.9}Mo_{0.1}O_{3-\delta}$ cathodes (denoted as SFO-SP and SFM–SP, respectively). Precursor solutions were prepared with stoichiometric amounts of metal nitrates $Fe(NO_3)_3 \cdot 9H_2O$ (Panreac 99.9%), $Sr(NO_3)_2$ (Aldrich 99.99%) and $(NH_4)_6Mo_7O_{24} \cdot 4H_2O$ (Aldrich 99.99%) and citric acid as a complexing agent, with a cation:citric acid molar ratio of 0.5:1 and concentration of 0.02 mol/L in distilled water. In contrast to the Pechini method, no polymerisation step is required in the spray-pyrolysis method. Pyrolysis occurs when pulverised drops contact the hot substrate, assisted by the combustion of the nitrates and citric acid in the solution. In the present case, the solutions were sprayed with a flow rate of 1 ml/min, over a $Ce_{0.9}Gd_{0.1}O_{2-\delta}$ (Rhodia, CGO)-based electrolyte heated at 350 °C. Densification of cylindrical pellets of the electrolyte was achieved by sintering at a temperature as low as 1100 °C for 6 h after the addition of a minor content of Co (2 mol%) following the methodology reported elsewhere [33]. After deposition, the electrolyte-electrode assemblies were heated at 850 °C for 1 h to crystallise the electrode and improve adherence with the electrolyte.

2.2. Structural and microstructural characterisation

Completeness of reaction and phase purity of SFO-P and SFM-P were firstly examined at RT by X-ray diffraction (XRD) using a Bruker D8 Advanced diffractometer, equipped with $CuK\alpha_1$ radiation ($\lambda = 1.5406$ Å) and germanium monochromator, in the range $20° \leq 2\theta \leq 70°$ employing a step increment of 0.02° and a step counting time of 1.5 s.

Neutron Powder Diffraction (NPD) as a function of temperature was employed for detailed structural analysis using the high-resolution D2B diffractometer at the Institut Laue-Langevin (ILL, Grenoble, France). Diffraction patterns were collected in air, using an open quartz tube, in the 2θ range RT-900 °C working at a wavelength $\lambda = 1.046531$ Å. The background from the quartz tube recorded at each temperature was subtracted from the corresponding pattern, prior to analysis by Rietveld refinement using the Fullprof software [34]. The refinements were performed fixing the Fe/Mo ratio and using isotropic thermal parameters for all atoms.

SFO-SP and SFM-SP deposited on CGO electrolytes by spray-pyrolysis were analysed by grazing incidence XRD in the range $27 \leq 2\theta \leq 48°$ with an increment of 0.02° step, using a Bruker D8 Advanced diffractometer, equipped with $CuK\alpha$ radiation and grazing incidence detector.

Microstructure and morphology of the samples were analysed by field-emission scanning electron microscopy (FE-SEM) with a Hitachi 4700s instrument coupled with energy-dispersive X-ray microanalysis (EDS-Noran). The grain size was analysed by the ImageJ software [35] using 10 FE-SEM images of different compositions (SFO–P, SFO-SP, SFM-P and SFM-SP), measuring fifty representative grains for each micrograph.

2.3. Air-electrode electrochemical analysis

Electrochemical characterisation was performed by impedance spectroscopy in the temperature range 550–800 °C using a 3-probe configuration with an external Pt-ring reference electrode located around the working electrode [36]. Synthesised powders of SFO-P and SFMO-P were mixed with a liquid binder (Decoflux™, WB41, Zschimmer and Schwartz) and brushed symmetrically on both faces of the CGO electrolyte to form internal circular electrodes of 5.5 mm in diameter and sintered at 1000 °C for 2 h. Internal circular electrodes were also directly deposited by spray pyrolysis (SFO-SP and SFMO-SP) over electrolyte substrates as indicated in Section 2.1. The as-prepared symmetrical electrodes were covered with Pt paint (Heraeus) and calcined at 800 °C to form current collectors.

Impedance spectra were collected in the frequency range $0.1–10^6$ Hz with a signal amplitude of 50 mV using an Autolab PGSTAT302N instrument with a FRA2 module (Metrohm). The effect of dc electrical current on the electrode performance was analysed under cathodic polarisation, in galvanostatic mode, in the current range 0–400 $mA \cdot cm^{-2}$ dc with a signal amplitude of 1 mA. The effects of thermal cycling on electrode degradation were determined by impedance spectroscopy in air in the range 300–800 °C employing ten heating/cooling cycles with 5 °C/min heating and cooling rate, using steps of 50 °C. Ageing of the electrodes was also evaluated by impedance spectroscopy at 700 °C for 100 h.

2.4. Fuel-cell preparation and performance analysis

Solid oxide single cells were fabricated employing an anode-supported configuration based on NiO-CGO composite as precursor anode, CGO as electrolyte and SFM-SP as cathode.

Applying the combustion method, NiO-CGO (60:40 wt %) composite powders were prepared by mixing stoichiometric amounts

of $Ni(NO_3)_2 \cdot 6H_2O$ (Sigma Aldrich 98.5%), $Ce(NO_3)_3$ (Aldrich 99.0%), $Gd(NO_3)_3$ (Aldrich 99.9%) and glycine as fuel, in an oxidiser-to-fuel ratio (φ = [(nitrate mols)x 5]/[(glycine mols) x 9]) of unity [37]. All reactants were dissolved in a minimum amount of water, and the solution heated in an oven at 500 °C for 1 h. The resulting ash-like powder was mixed with glassy carbon microspheres (15 vol %, Sigma Aldrich 99.9%) to achieve a suitable level of porosity. The blend was milled in a Fritsch pulverisette planetary ball mill at 200 rpm with reverse rotation, employing 6 cycles of 5 min in duration, with 2 min pause between cycles.

The NiO-CGO-C mixture was pressed into a pellet of diameter 12 mm and thickness 1 mm, which was then fired at 1000 °C for 1 h to burn off the carbon and obtain a porous disc. An ink was prepared by mixing CGO powder with a binder (Decoflux™, WB41, Zschimmer and Schwartz) to form a slurry, which was painted over the surface of the NiO-CGO pellet and sintered at 1450 °C for 6 h to obtain a dense, thin electrolyte. Preparation and deposition of the SFM-SP cathode over the CGO electrolyte were performed by spray pyrolysis following the procedure mentioned above (section 2.1).

Current collectors were prepared by covering the cathode and the anode with Pt ink (Heraeus) and calcining at 800 °C for 1 h followed by attachment of pairs of Pt wires to the anode and cathode.

Fuel-cell performance was studied with an in-house test set-up. The single cell was sealed over a YSZ tube by means of a Ceramabond 552 adhesive (Aremco), providing a circular active surface of diameter 7.5 mm. Ni-CGO cermet anode was obtained by in-situ reduction of NiO under a H_2 flow rate of 50 ml/min for 2 h on the anode side. Fuel-cell performance was evaluated in the range 650–800 °C on supplying dry H_2 to the anode and air to the cathode at flow rates 50 ml/min. Current-voltage behaviour was studied with an Autolab PGSTAT302N potentiostat/galvanostat (Metrohm).

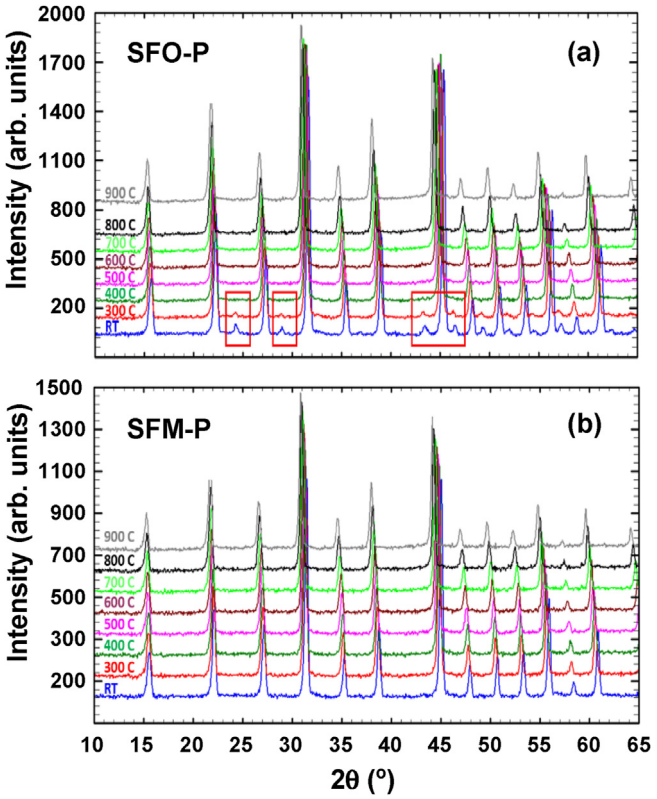

Fig. 1. NPD patterns of (a) SFO-P and (b) SFM-P in the range RT- 900 °C. Note that some peaks of SFO-P indicated in (a) disappear at 400 °C corresponding to the tetragonal-to-cubic phase transition.

3. Results and discussion

3.1. Structural and microstructural analysis

Room temperature XRD powder patterns of SFO-P and SFM-P confirmed the formation of single-phase perovskite after heat treatment at 1000 °C for 10 h. Tetragonal (space group I4/mcm) and orthorhombic (Cmmm) symmetries produced very similar Rietveld refinements for SFO-P, whereas SFM-P was successfully refined in cubic symmetry (Pm-3m), as reported previously [31].

In the case of perovskites with different symmetries arising from minor distortions, the greater neutron scattering factor of oxygens in comparison to that of X-rays means that symmetry determination and oxygen content may be more successfully performed via neutron diffraction. Hence, in the present case, an analysis of the structural behaviour of $SrFeO_{3-\delta}$ and $SrFe_{0.9}Mo_{0.1}O_{3-\delta}$ as a function of temperature was performed by Rietveld refinement of neutron powder diffraction data.

Fig. 1 shows the temperature evolution of NPD patterns for SFO-P (Fig. 1(a)) and SFM-P (Fig. 1(b)); a limited zone of the NPD patterns is plotted for the sake of clarity. Figs. S1–S16 display the fitting results of all NPD patterns refined with the structural models given in Tables S1 and S2 for SFO-P and SFM-P, respectively. At RT, SFO-P exhibits a tetragonal structure (S.G. I4/mcm) due to ordering of oxygen vacancies, which was previously observed at RT for an oxygen content of 2.85 per formula unit [38].

On heating, the tetragonal structure remains up to 300 °C (Fig. 2(a)), above which cubic perovskite forms (S.G. Pm-3m) due to disordering of oxygen vacancies. The phase transition occurs around 400 °C (Fig. 2(b)) and the cubic structure is stable up to 900 °C (Figs. S3–S8). In contrast, the Mo-containing compound (SFM-P) is cubic in the entire studied range, RT-900 °C (Fig. 2(c) and Figs. S9–S16), and possesses a significantly larger oxygen content, as reported previously [31], attributable to the high oxidation state of Mo (VI). The random distribution of Mo and Fe ions in the perovskite B site most likely leads to a random distribution of oxygen vacancies associated with cubic symmetry. The much higher concentration of vacancies in the anionic substructure of SFO-P may result in poor long-term material stability.

The thermal evolution of the unit-cell volume of SFO-P determined from NPD refinement, Fig. 3, exhibits a linear increase with increasing temperature in the range RT-300 °C (Fig. 3(a)). The cell volume undergoes a contraction in the range 300–400 °C associated to the transition from tetragonal to cubic symmetry (Fig. 2)), then increases linearly once more as temperature increases further (400–900 °C). The linear expansion is greater in the high-temperature range in comparison to that at low-temperature, corresponding to rapid oxygen loss at about 400 °C, previously determined by thermogravimetry [31], thereby reducing the B-site cations which adopt a higher average ionic radii. Although the Mo-doped composition exhibits cubic symmetry in the entire range RT-900 °C, the volume expansion as a function of temperature also exhibits a greater slope for temperatures higher than ~400 °C (Fig. 3(b)), again ascribed to abrupt oxygen loss and the concomitant reduction of B-site cations. The volume expansions determined by NPD are consistent with the thermal-expansion behaviour previously determined by dilatometry and confirm lower values of thermal expansion coefficients for SFM-P in comparison to SFO-P (Fig. 3), due to the lower content of the larger Fe^{3+} ions in SFM-P and the stronger Mo–O bond in comparison to that of Fe–O, which is apparent from the lower oxygen loss on heating obtained for SFM-P (Tables S1 and S2).

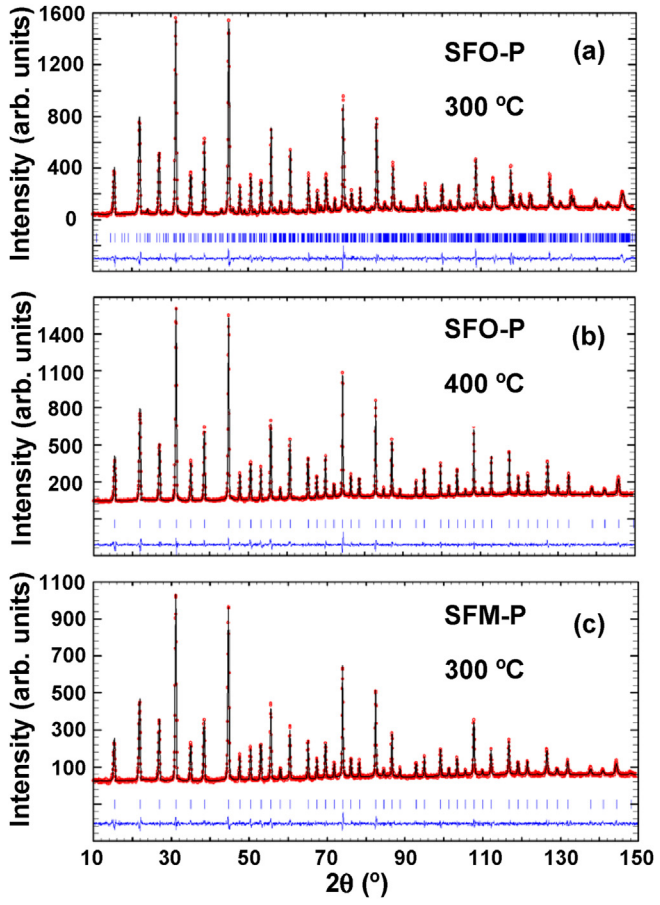

Fig. 2. Observed (circles), calculated (continuous line) and difference (continuous line at bottom) NPD profiles for SFO-P at 300 °C (a) and 400 °C (b) and for SFM-P at 300 °C (c); vertical bars indicate the expected position of Bragg peaks. The corresponding structural models are given in Tables S1 and S2.

The grazing-incidence-XRD patterns of $SrFeO_{3-\delta}$ (SFO-SP) and $SrFe_{0.9}Mo_{0.1}O_{3-\delta}$ (SFM-SP), deposited by spray pyrolysis over CGO electrolyte and treated at 850 °C for 1 h, confirm single phase compositions (Fig. S17), with a displacement of diffraction peaks to lower angles in SFM-SP compared to SFO-SP, as observed previously [39], which is ascribed to the introduction of Mo species in the perovskite structure, and the corresponding cell expansion. The reflections are of insufficient resolution to differentiate between tetragonal and cubic symmetries.

SEM images of Mo-doped compositions prepared by the modified Pechini method and spray pyrolysis, deposited over CGO electrolytes, and sintered in air at 1000 °C for 10 h and 850 °C for 2 h, respectively, are presented in Fig. 4. Energy-dispersive-X-ray spectroscopy of the cross-section of the symmetrical cells used for impedance spectroscopy analysis (Fig. 4(a) and (c)) shows well defined layers corresponding to the Pt current collector (yellow), Sr from the electrode (red) and Ce from the electrolyte (blue). Fig. S18 confirms that Pt remains over the top surface of the cathode, improving electrical current collection, without producing any catalytic activity within the electrode bulk volume of SFM-SP, where it is absent. The magnified SEM images (Fig. 4(b) and (d)) reveal the lower grain size, higher porosity and better-connected grains of the spray-pyrolysed material in comparison to the material synthesised by the modified Pechini route.

The grain-size distributions, determined from the corresponding SEM images are shown in Fig. 4(e)–(h).

The materials prepared by the Pechini process present lower grain sizes than similar systems prepared by different synthesis routes [40,41]. However, grain-size distributions are still lower for the samples prepared by spray pyrolysis. On the other hand, Mo-doped samples exhibit a greater grain size in both methods of processing. Compositions prepared by spray pyrolysis present narrower distributions around the average values, associated to the very good particle homogeneity.

3.2. Electrochemical properties

Fig. 5(a) shows the Arrhenius representation of the electrode-polarisation resistance (R_p) evaluated without application of a d.c. signal. The spray-pyrolysed materials exhibit a significant reduction of R_p compared to the Pechini-based analogues, most likely attributable to the smaller grain size and improved particle homogeneity, resulting in a higher electrochemical surface area associated to the bulk electrode. On the other hand, the ohmic contribution of half cells (Fig. S19) also decreases for the spray-pyrolysis samples compared to the Pechini-prepared analogues, which indicates that there is a greater interface contact of the former with the electrolyte (Fig. 4), enhancing electrode-electrolyte ionic transfer and enlarging the active region. However, this enhancement is comparatively lower than that of the R_p, which suggests that the higher electrode-active area associated to the lower grain size of the spray-pyrolysis samples is principally

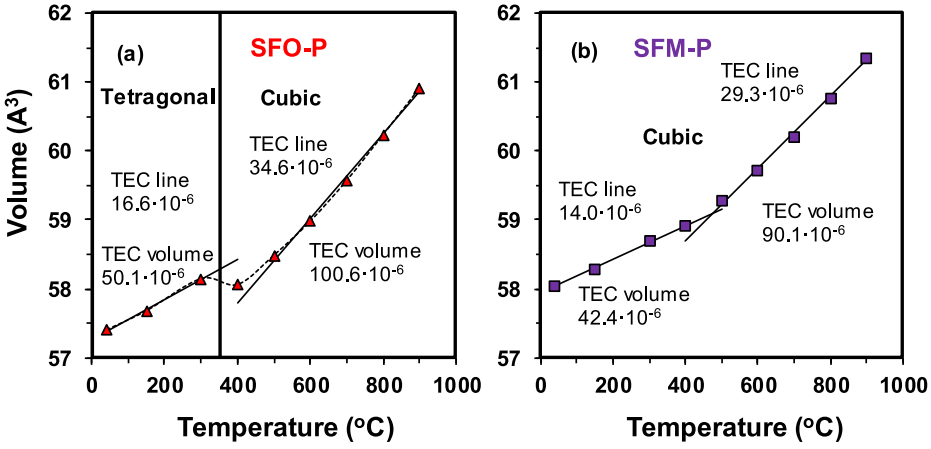

Fig. 3. Temperature dependence of unit-cell volume for $SrFeO_{3-\delta}$ (a) and $SrFe_{0.9}Mo_{0.1}O_{3-\delta}$ (b), determined from NPD data.

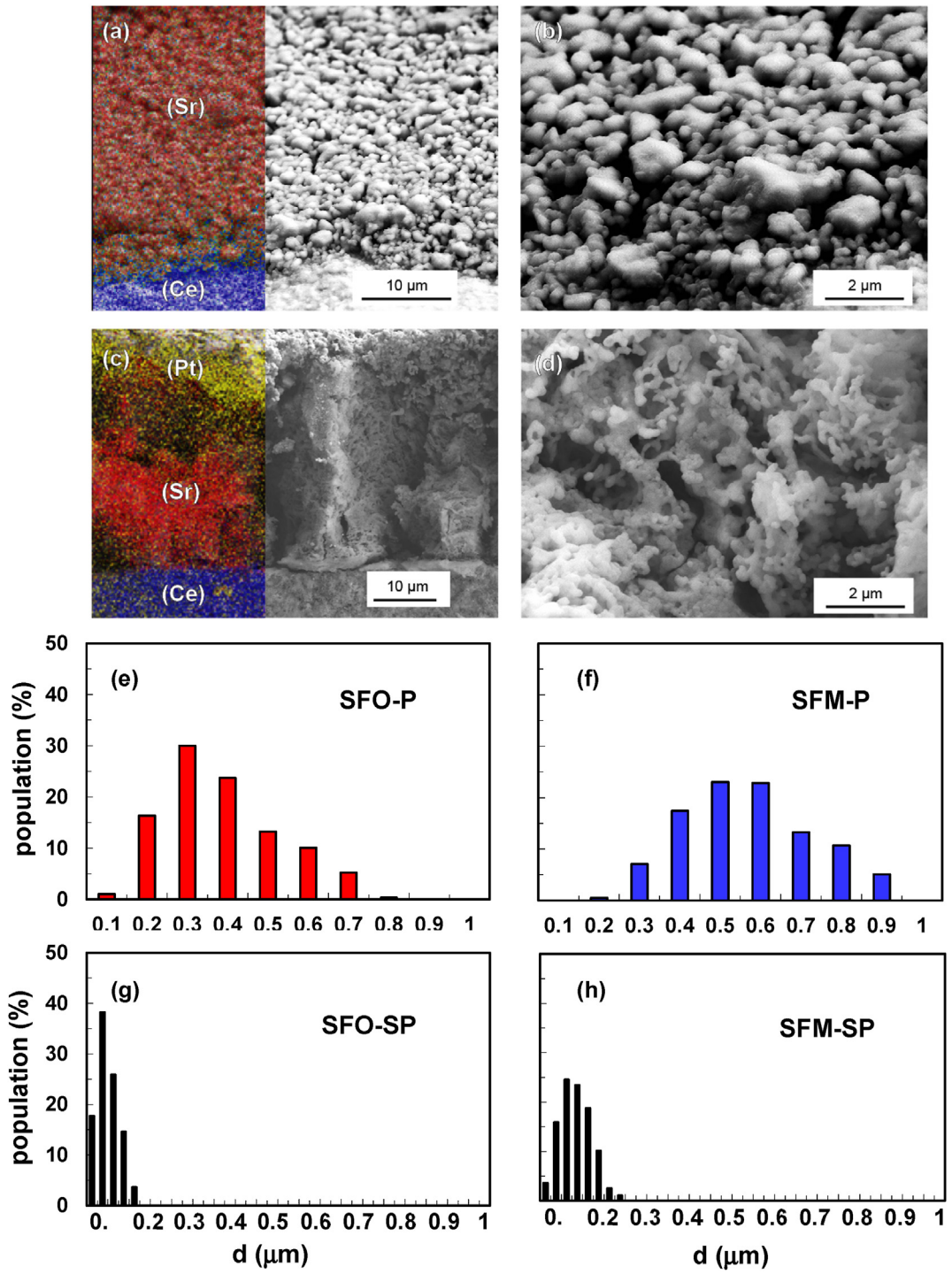

Fig. 4. SEM-EDXS cross-sectional images of $SrFe_{0.9}Mo_{0.1}O_{3-\delta}$ prepared by a modified Pechini method (a,b) and spray pyrolysis (c,d) deposited on CGO electrolyte, with Pt as current collector; grain-size distributions of compositions synthesised by the modified Pechini method (e, f) and spray pyrolysis (g, h), for $SrFeO_{3-\delta}$ (e, g) and $SrFe_{0.9}Mo_{0.1}O_{3-\delta}$ (f, h).

responsible for their improved performance. Similar activation energies in the range 1.34–1.40 eV were obtained for the different samples (Fig. 5(a)), indicating that the similar compositions and structures give rise to analogous electrochemical mechanisms.

Impedance spectra at 700 °C in air (Fig. 5(b)) show that the electrode polarisation resistance of spray-pyrolysed $SrFeO_{3-\delta}$ decreases from 0.55 to 0.19 Ω cm_2 when compared to the sample prepared by Pechini. In the case of the $SrFe_{0.9}Mo_{0.1}O_{3-\delta}$ electrode, the corresponding drop is greater still for the spray-pyrolysed sample, from 0.42 to 0.11 Ω cm^2. Deposition of the air electrodes by spray pyrolysis thus significantly enhances the electrochemical performance, achieving electrode-polarisation resistances comparable or even better than those reported for Sr-based cobaltite systems [42–46].

Fig. 5(c) and (d) show the effect of dc cathodic current on the electrode polarisation resistance of SFO-SP and SFM-SP in the range 600–800 °C. The electrochemical behaviour is more affected by dc current at lower temperature, showing a considerable decrease of

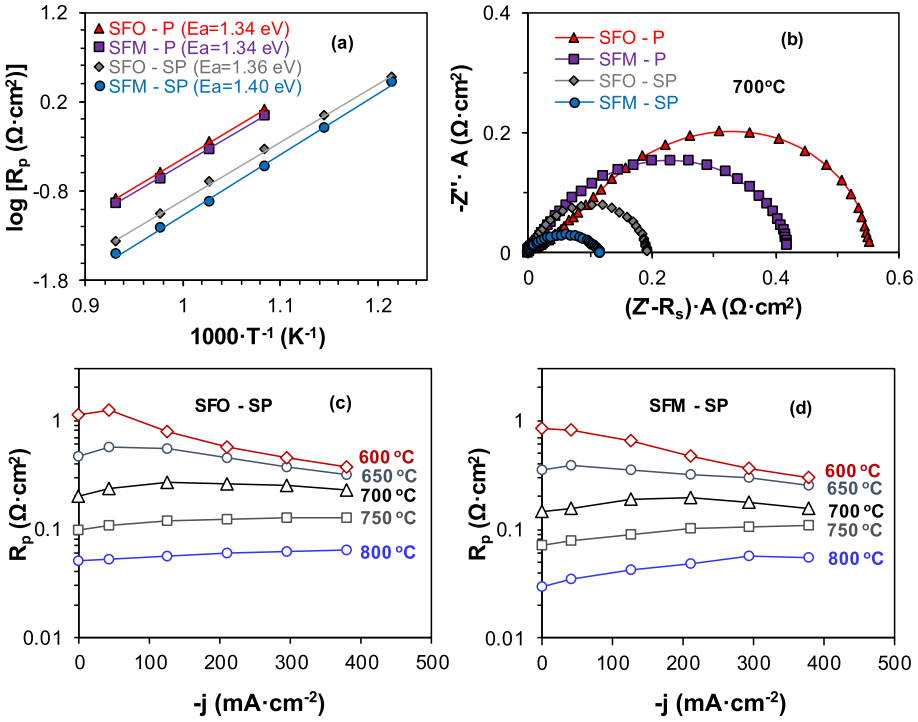

Fig. 5. Arrhenius representation of electrode polarisation resistance (a) and impedance spectra at 700 °C (b), of SFO-P (triangles), SFM-P (squares), SFO-SP (diamonds) and SFM-SP (circles); effect of dc cathodic current density on electrode polarisation resistance for SFO-SP (c) and SFM-SP (d) in the range 600–800 °C. Note that in (b) the electrolyte contribution has been subtracted from the Z′ axis of the impedance spectra for a better comparison of the electrode polarisation.

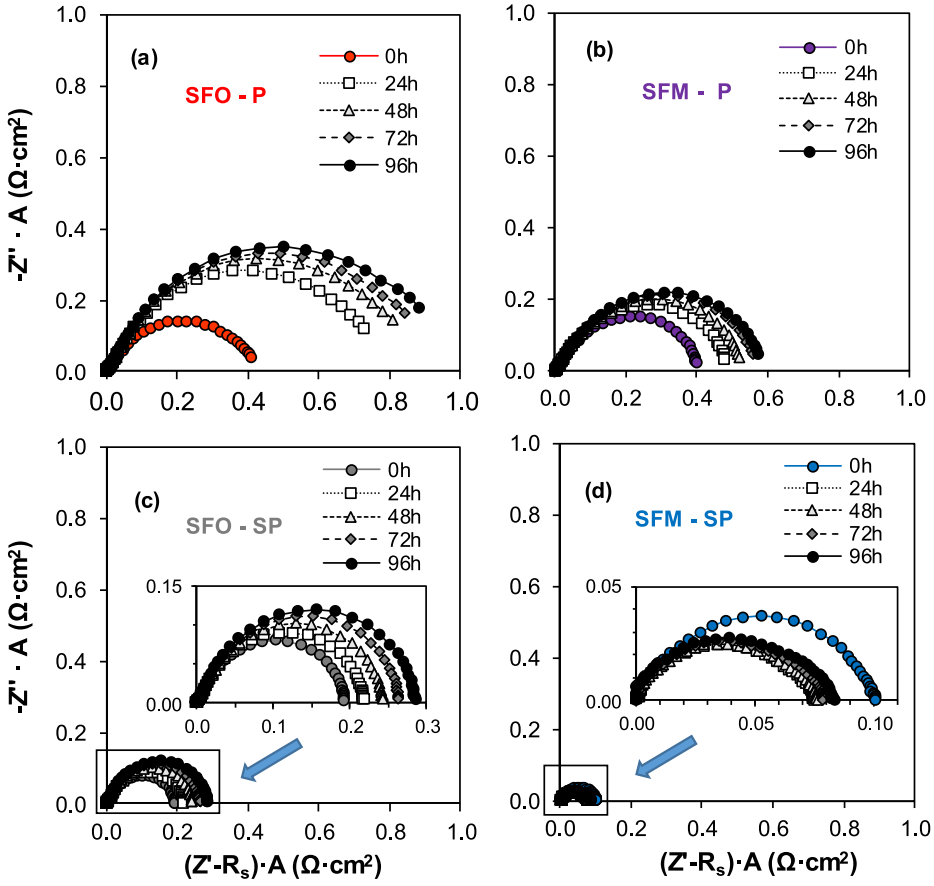

Fig. 6. Impedance spectra for different ageing periods for (a) SFO-P, (b) SFM-P, (c) SFO-SP and (d) SFM-SP, at 700 °C.

the electrode polarisation resistance at 600 °C, with only minor modifications for higher temperatures in the range 650–800 °C. The behaviour is very similar to that previously reported for Pechini-prepared material [31] and similar compositions [44,46], and was demonstrated to be highly dependent on the mixed ionic-electronic transport properties of the corresponding cathode material [36]. In this regard, it is known that the electrochemical activity of oxygen in mixed ionic-electronic materials comprises the surface exchange of oxygen and the bulk diffusion of oxide ions [47,48]. In addition to the oxygen bulk diffusion, oxygen surface exchange is also dominated by oxygen vacancies, since the surface reaction involves an ion-site exchange [48]. In the low temperature range, oxide-ion diffusion and the oxygen exchange are slower, leading to a greater concentration of oxygen vacancies at reaction sites for higher current densities. In contrast, in the high temperature range, both parameters are faster and the oxygen-vacancy concentration at reaction sites is less affected by dc polarisation. These considerations lead to an increased current dependence of the electrode polarisation resistance in the low temperature range, as observed in Fig. 5 (c) and (d).

3.3. Stability study

Electrochemical stability of the air electrodes was analysed by impedance spectroscopy without dc bias for 100 h using the corresponding half-cells in three-electrode configuration (Fig. 6). The electrode polarisation resistance of the Pechini-prepared samples SFO-P and SFM-P increased with time of exposure, rising from 0.4 to 1 Ω cm^2 (Fig. 6(a)) and from 0.4 to 0.6 Ω cm^2 (Fig. 6(b)), respectively, after 100 h of ageing.

Both of the spray-pyrolysed samples present higher stabilities (Fig. 6(c) and (d)). In particular, the electrode polarisation resistance of SFM-SP is very stable, decreasing slightly from 0.1 Ω cm^2 to 0.085 Ω cm^2 during the first 10 h and then remaining steady during the following 90 h of ageing (Fig. 7(a)). The enhancement observed during the first interval of exposure was reported previously, and is attributable to interfacial rearrangement [44]. The greater stability observed for the spray-pyrolysed samples has previously been observed for several cathode compositions, such as $La_{0.6}Sr_{0.4}Co_{0.2}Fe_{0.8}O_{3-\delta}$ [49] and $PrBaCo_2O_{5+\delta}$ [50]. Although we did not find any apparent evidence by SEM, this improvement may result from less microstructural modification or coarsening, which is well documented to produce long-term instabilities [47], in addition to an optimised interface homogeneity, which facilitates the electrochemical reaction (Fig. 4(b) and (d)). Moreover, L. dos Santos et al. [49] indicated that the lower stability of the conventionally prepared samples may be ascribed to a greater degree of A-site cation segregation. It was argued that the greater crystallinity associated with the higher synthesis temperature produces a more orderly arrangement with less free space, which drives larger cations to the cathode surface. The ohmic contribution of the different samples remained essentially constant during time-degradation tests (Fig. S20). In addition, ageing was evaluated at 700 °C by impedance spectroscopy with an applied dc cathodic current of 379 mA cm^{-2} for 75 h for the SFM-SP sample. The results confirm that the electrode polarisation resistance remains constant under dc polarisation, with values very similar to those obtained in the absence of cathodic bias (Fig. S21).

The stability of the prepared compositions was also studied on assessing the electrode performance at 700 °C after 10 heating/cooling cycles in the range 300–800 °C, Fig. 7(b). Consistent with the ageing study, Mo doping enhances stability in both types of processed samples, which may be because the same symmetry is retained in the cycled temperature range, as confirmed by NPD (Fig. 2 and Figs. S9–S16). On the other hand, the R_p of SFM-SP decreases during the first 7 cycles and remains stable thereafter. Hence, as is the case in the ageing study, the spray-pyrolysed compositions present a higher cycling stability than the homologous compositions prepared by the traditional modified Pechini procedure.

It is apparent from Figs. 6 and 7 that there is a greater degradation of $SrFeO_{3-\delta}$ compared to $SrFe_{0.9}Mo_{0.1}O_{3-\delta}$, independent of the experimental procedure. This may be related to the very low oxygen content of $SrFeO_{3-\delta}$ [31], and the corresponding phase transition and lattice distortion [51], all of which are redressed on Mo doping. Moreover, the potential of the spray-pyrolysis fabrication route for optimising electrochemical performance and stability of air electrodes for solid oxide fuel cells is demonstrated.

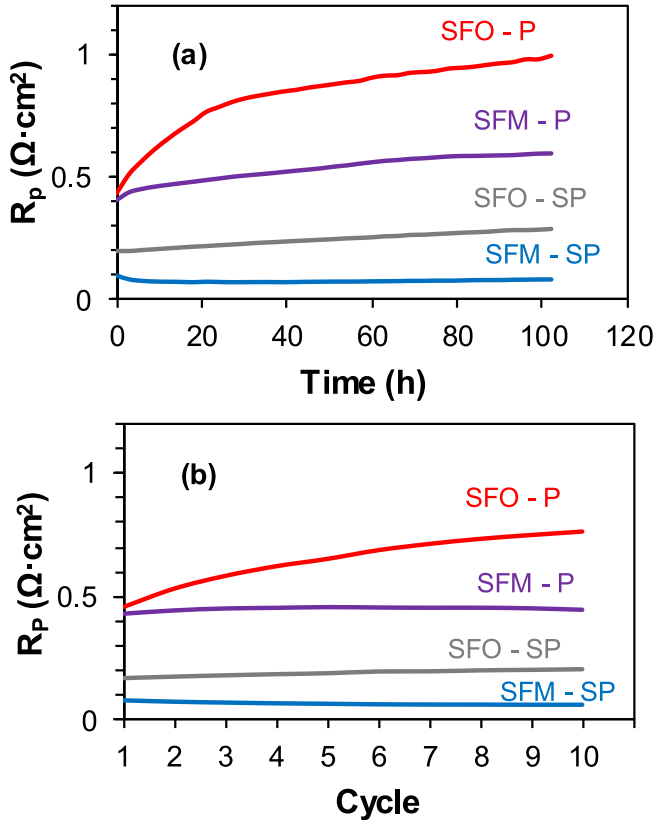

Fig. 7. Electrode polarisation resistance at 700 °C as a function of time of exposure (a) and as a function of the number of heating/cooling cycles (b).

3.4. Fuel-cell test

Fuel-cell performance was evaluated on a Ni-CGO anode-supported single cell with CGO electrolyte and SFM-SP cathode, using H_2 as fuel and air as oxidant.

Voltage and power density curves as a function of current density are shown in Fig. 8(a). The open-circuit voltage is affected by electronic leakage from the CGO thin electrolyte and is considerably lower than the Nernst voltage for pure ionic conductors, showing values of 0.86, 0.81 and 0.67 V for 650, 700 and 800 °C, respectively. However, the good performance of the spray-pyrolysed air electrodes produces power densities of 0.3, 0.5 and 0.9 W cm^{-2} at 650, 700 and 800 °C, respectively. An SEM image of the single cell after the fuel-cell test (Fig. 8 (b)) shows a very dense electrolyte with an average thickness of approximately 30–35 μm (Fig. 8 (c)). Both the anode and the cathode present very good porosity and particle homogeneity, which facilitates H_2 and O_2 distribution and diffusion. Moreover, the interfaces between both

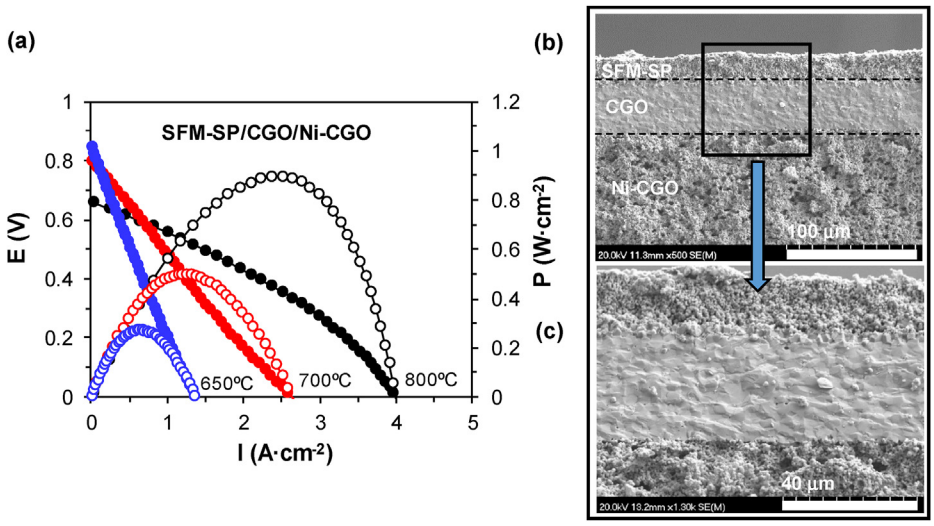

Fig. 8. (a) Fuel-cell performance of an anode-supported single cell based on SFM-SP/CGO/Ni-CGO using H_2 as fuel and air as oxidant; (b)–(c) post-mortem SEM image of the single cell.

electrodes and the electrolyte show very good adherence, with no signs of degradation after the fuel-cell test. The cost-effectiveness and scalability of spray pyrolysis, together with the high performance and stability of the air electrodes demonstrated in this study, confirm the considerable potential of this deposition method for the fabrication of electrodes for solid oxide fuel cells.

4. Conclusions

Molybdenum was confirmed as an efficient dopant for phase stabilisation and electrochemical enhancement of $SrFeO_{3-\delta}$ cathodes. Neutron powder diffraction of samples prepared by a Pechini-based method indicated that undoped $SrFeO_{3-\delta}$ presents a tetragonal phase from room temperature to 300 °C, with a phase transition to cubic symmetry occurring at 400 °C. In contrast, $SrFe_{0.9}Mo_{0.1}O_{3-\delta}$ exhibits cubic symmetry from RT to 900 °C, most likely resulting from a higher oxygen content.

Synthesis of cathode layers by spray pyrolysis considerably enhances electrochemical performance, attributable to improved homogeneity, distribution and adhesion, and lower grain size. Moreover, spray-pyrolysed compositions offer considerable improvement of the electrochemical stability on isothermal ageing and under several heating/cooling cycles. The electrochemical performance of $SrFe_{0.9}Mo_{0.1}O_{3-\delta}$ prepared by spray pyrolysis showed no evidence of degradation after 100 h of exposure to air at 700 °C and after 10 heating/cooling cycles between 300 and 800 °C.

A fuel-cell test of a single cell based on spray-pyrolysed $SrFe_{0.9}Mo_{0.1}O_{3-\delta}$, deposited over a thin CGO electrolyte and a Ni-CGO anode support, exhibited power densities of 0.5 and 0.9 W cm^{-2} at 700 and 800 °C, respectively, which are comparable to values obtained in similar Co-based perovskites. Spray pyrolysis is thus a promising cost-effective procedure to prepare cobalt-free compositions with optimised performance and stability.

CRediT authorship contribution statement

Víctor Zapata-Ramírez: Investigation, Methodology, Formal analysis, Writing – original draft. **Paula Rosendo-Santos:** Investigation, Methodology. **Ulises Amador:** Validation, Investigation, Writing – review & editing. **Clemens Ritter:** Investigation, Writing – review & editing. **Glenn C. Mather:** Conceptualization, Writing – review & editing, Supervision, Project administration, Funding acquisition. **Domingo Pérez-Coll:** Formal analysis, Writing – review & editing, Supervision, Project administration, Funding acquisition.

Declaration of competing interest

The authors declare that they have no known competing financial interests or personal relationships that could have appeared to influence the work reported in this paper.

Acknowledgements

The authors acknowledge the Fundación Domingo Martínez ("Ayuda a la Investigación 2017. Área de Materiales: celdas de combustible") and "Ministerio de Ciencia, Innovación y Universidades" (RTI2018-095088-B-I00) for financial support. We also thank the Spanish MICINN and the Agencia Estatal de Investigación (AEI)/Fondo Europeo de Desarrollo Regional (FEDER/UE) for funding the Project PID2019-106662RB-C41. UA and PRS thank University San Pablo CEU (USP CEU) for financial support. We thank Institut Laue-Langevin (ILL) for allocation of beam time (experiment code 5-21-1132 https://doi.org/10.5291/ILL-DATA. 5-21-1132). We acknowledge support of the publication fee by the CSIC Open Access Publication Support Initiative through its Unit of Information Resources for Research (URICI).

Appendix A. Supplementary data

Supplementary data to this article can be found online at https://doi.org/10.1016/j.renene.2021.12.121.

References

[1] United Nations General Assembly, Resolution Adopted by the General Assembly on 25 September 2015, 70/1. Transforming Our World: the 2030 Agenda for Sustainable Development.
[2] D.J.L. Brett, A. Atkinson, N.P. Brandon, S.J. Skinner, Intermediate temperature solid oxide fuel cells, Chem. Soc. Rev. 37 (2008) 1568–1578, https://doi.org/10.1039/b612060c.
[3] F. Ramadhani, M.A. Hussain, H. Mokhlis, S. Hajimolana, Optimization strategies for solid oxide fuel cell (SOFC) application: a literature survey, Renew. Sustain. Energy Rev. 76 (2017) 460–484, https://doi.org/10.1016/J.RSER.2017.03.052.
[4] A.M. Abdalla, S. Hossain, P.M. Petra, M. Ghasemi, A.K. Azad, Achievements and trends of solid oxide fuel cells in clean energy filed: a perspective review, Front. Energy 14 (2020) 359–382, https://doi.org/10.1007/s11708-018-0546-2.

[5] N. Mahato, A. Banerjee, A. Gupta, S. Omar, K. Balani, Progress in material selection for solid oxide fuel cell technology: a review, Prog. Mater. Sci. 72 (2015) 141–337, https://doi.org/10.1016/j.pmatsci.2015.01.001.

[6] L. Zhang, G. Chen, R. Dai, X. Lv, D. Yang, S. Geng, A review of the chemical compatibility between oxide electrodes and electrolytes in solid oxide fuel cells, J. Power Sources 492 (2021) 229630, https://doi.org/10.1016/j.jpowsour.2021.229630.

[7] A. Jun, J. Kim, J. Shin, G. Kim, Perovskite as a cathode material: a review of its role in solid-oxide fuel cell technology, ChemElectroChem 3 (2016) 511–530, https://doi.org/10.1002/celc.201500382.

[8] J.M. Porras-Vazquez, T. Pike, C.A. Hancock, J.F. Marco, F.J. Berry, P.R. Slater, Investigation into the effect of Si doping on the performance of $SrFeO_{3-\delta}$ SOFC electrode materials, J. Mater. Chem. A 1 (2013) 11834–11841, https://doi.org/10.1039/c3ta12113e.

[9] L. Bian, C. Liu, S. Li, J. Peng, X. Li, L. Guan, Y. Liu, J.H. Peng, S. An, X. Song, Highly stable $La_{0.5}Sr_{0.5}Fe_{0.9}Mo_{0.1}O_{3-\delta}$ electrode for reversible symmetric solid oxide cell, Int. J. Hydrogen Energy 45 (2020) 19813–19822, https://doi.org/10.1016/j.ijhydene.2020.05.117.

[10] J. Zamudio-García, J.M. Porras-Vázquez, L. dos Santos-Gómez, E.R. Losilla, D. Marrero-López, Effect of Zn addition on the structure and electrochemical properties of co-doped $BaCe_{0.6}Zr_{0.2}Ln_{0.2}O_{3-\delta}$ (Ln=Y, Gd, Yb) proton conductors, Ceram. Int. 44 (2018) 14113–14121, https://doi.org/10.1016/j.ceramint.2018.05.010.

[11] D. Ding, X. Li, S.Y. Lai, K. Gerdes, M. Liu, Enhancing SOFC cathode performance by surface modification through infiltration, Energy Environ. Sci. 7 (2014) 552–575, https://doi.org/10.1039/C3EE42926A.

[12] W.H. Kan, A.J. Samson, V. Thangadurai, Trends in electrode development for next generation solid oxide fuel cells, J. Mater. Chem. A. 4 (2016) 17913–17932, https://doi.org/10.1039/C6TA06757C.

[13] L. Fan, B. Zhu, P.-C. Su, C. He, Nanomaterials and technologies for low temperature solid oxide fuel cells: recent advances, challenges and opportunities, Nano Energy 45 (2018) 148–176, https://doi.org/10.1016/J.NANOEN.2017.12.044.

[14] L. dos Santos-Gómez, J.M. Porras-Vázquez, F. Martín, J.R. Ramos-Barrado, E.R. Losilla, D. Marrero-López, A novel multilaminated composite cathode for solid oxide fuel cells, Ceram. Int. 45 (2019) 18124–18127, https://doi.org/10.1016/j.ceramint.2019.05.296.

[15] C. Zhao, Y. Li, W. Zhang, Y. Zheng, X. Lou, B. Yu, J. Chen, Y. Chen, M. Liu, J. Wang, Heterointerface engineering for enhancing the electrochemical performance of solid oxide cells, Energy Environ. Sci. 13 (2020) 53–85, https://doi.org/10.1039/c9ee02230a.

[16] S. Kye, H.J. Kim, D. Go, B.C. Yang, J.W. Shin, S. Lee, J. An, Ultralow-loading ruthenium catalyst by plasma-enhanced atomic layer deposition for solid oxide fuel cell, ACS Catal. 11 (2021) 3523–3529, https://doi.org/10.1021/acscatal.0c04526.

[17] V. Zapata-Ramírez, L. dos Santos-Gómez, G.C. Mather, D. Marrero-López, D. Pérez-Coll, Enhanced intermediate-temperature electrochemical performance of air electrodes for solid oxide cells with spray-pyrolized active layers, ACS Appl. Mater. Interfaces 12 (2020), 10571-10578. doi:10.1021/acsami.9b22966.

[18] J. Zamudio-García, N. Albarrán-Aroca, J.M. Porras-Vázquez, E.R. Losilla, D. Marrero-López, Influence of $Bi_{1.5}Y_{0.5}O_3$ active layer on the performance of nanostructured $La_{0.8}Sr_{0.2}MnO_3$ cathode, Appl. Nano. 1 (2020) 14–24, https://doi.org/10.3390/applnano1010003.

[19] B. Kamecki, J. Karczewski, P. Jasiński, S. Molin, Improvement of oxygen electrode performance of intermediate temperature solid oxide cells by spray pyrolysis deposited active layers, Adv. Mater. Interfac. (2021) 2002227, https://doi.org/10.1002/admi.202002227.

[20] E.-L. Ruokonen, M. Linnainmaa, M. Seuri, P. Juhakoski, K.-O. Söderström, A fatal case of hard-metal disease, Scand. J. Work. Environ. Health 22 (1996) 62–65, https://doi.org/10.5271/sjweh.111.

[21] S.H. Farjana, N. Huda, M.A.P. Mahmud, Life cycle assessment of cobalt extraction process, J. Sustain. Mining 18 (2019) 150–161, https://doi.org/10.1016/j.jsm.2019.03.002.

[22] Y. Zhao, X. Gao, H. An, X. Xi, Q. Sun, M. Jiang, The effect of the mined cobalt trade dependence Network's structure on trade price, Resour. Pol. 65 (2020) 101589, https://doi.org/10.1016/j.resourpol.2020.101589.

[23] L. dos Santos-Gómez, J.M. Compana, S. Bruque, E.R. Losilla, D. Marrero-López, Symmetric electrodes for solid oxide fuel cells based on Zr-doped $SrFeO_{3-\delta}$, J. Power Sources 279 (2015) 419–427, https://doi.org/10.1016/j.jpowsour.2015.01.043.

[24] N.A. Baharuddin, N.A. Mohd Nazrul Aman, A. Muchtar, M.R. Somalu, A.A. Samat, M.I. Aznam, Structural, morphological and electrochemical behaviour of titanium-doped $SrFe_{1-x}Ti_xO_{3-\delta}$ (x=0.1-0.5) perovskite as cobalt-free solid oxide fuel cell cathode, Ceram. Int. 45 (2019) 12903–12909, https://doi.org/10.1016/j.ceramint.2019.03.216.

[25] C. Yao, H. Zhang, X. Liu, J. Meng, J. Meng, F. Meng, A niobium and tungsten co-doped $SrFeO_{3-\delta}$ perovskite as cathode for intermediate temperature solid oxide fuel cells, Ceram. Int. 45 (2019) 7351–7358, https://doi.org/10.1016/j.ceramint.2019.01.019.

[26] Y. Meng, L. Sun, J. Gao, W. Tan, C. Chen, J. Yi, H.J.M. Bouwmeester, Z. Sun, K.S. Brinkman, Insights into the CO_2 stability-performance trade-off of antimony-doped $SrFeO_{3-\delta}$ perovskite cathode for solid oxide fuel cells, ACS Appl. Mater. Interfaces 11 (2019) 11498–11506, https://doi.org/10.1021/acsami.9b00876.

[27] C. Yao, J. Yang, S. Chen, J. Meng, K. Cai, Q. Zhang, Copper doped $SrFe_{1-x}Cu_xW_{0.1}O_{3-\delta}$ (x=0-0.3) perovskites as cathode materials for IT-SOFCs, J. Alloys Compd. 868 (2021) 159127, https://doi.org/10.1016/j.jallcom.2021.159127.

[28] N.A. Baharuddin, A. Muchtar, M.R. Somalu, Preparation of $SrFe_{0.5}Ti_{0.5}O_{3-\delta}$ perovskite-structured ceramic using the glycine-nitrate combustion technique, Mater. Lett. 194 (2017) 197–201, https://doi.org/10.1016/j.matlet.2017.02.064.

[29] Shanshan Jiang, Jaka Sunarso, Wei Zhou, Jian Shen, Ran Ran, Zongping Shao, Cobalt-free $SrNb_xFe_{1-x}O_{3-\delta}$ (x= 0.05, 0.1 and 0.2) perovskite cathodes for intermediate temperature solid oxide fuel cells, J. Power Sources 298 (2015) 209–216, https://doi.org/10.1016/j.jpowsour.2015.08.063.

[30] G. Hong, T.W. Kim, M.J. Kwak, J. Song, Y. Choi, S.-K. Woo, M.H. Han, C.H. Cho, S.-D. Kim, Composite electrodes of Ti-doped $SrFeO_{3-\delta}$ and LSGMZ electrolytes as both the anode and cathode in symmetric solid oxide fuel cells, J. Alloys Compd. 846 (2020) 156154, https://doi.org/10.1016/j.jallcom.2020.156154.

[31] V. Zapata-Ramírez, G.C. Mather, M.T. Azcondo, U. Amador, D. Pérez-Coll, Electrical and electrochemical properties of the $Sr(Fe,Co,Mo)O_3$ system as air electrode for reversible solid oxide cells, J. Power Sources 437 (2019) 226895, https://doi.org/10.1016/j.jpowsour.2019.226895.

[32] M.P. Pechini, Method of Preparing Lead and Alkaline Earth Titanates and Niobates and Coating Method Using the Same to Form a Capacitor, US Pat. No. 3330697, 1967. (n.d.).

[33] D. Pérez-Coll, P. Núñez, J.R. Frade, J.C.C. Abrantes, Conductivity of CGO and CSO ceramics obtained from freeze-dried precursors, Electrochim. Acta 48 (2003) 1551–1557, https://doi.org/10.1016/S0013-4686(03)00027-6.

[34] J. Rodríguez-Carvajal, Recent advances in magnetic structure determination by neutron powder diffraction, Phys. B Condens. Matter 192 (1993) 55–69, https://doi.org/10.1016/0921-4526(93)90108-I.

[35] W.S. Rasband, ImageJ, U. S. National Institutes of Health, Bethesda, Maryland, USA, 1997–2011.

[36] D. Pérez-Coll, A. Aguadero, M.J. Escudero, L. Daza, Effect of DC current polarization on the electrochemical behaviour of $La_2NiO_{4+\delta}$ and $La_3Ni_2O_{7+\delta}$-based systems, J. Power Sources 192 (2009) 2–13, https://doi.org/10.1016/j.jpowsour.2008.10.073.

[37] S.R. Jain, K.C. Adiga, V.R. Pai Verneker, A new approach to thermochemical calculations of condensed fuel-oxidizer mixtures, Combust. Flame 40 (1981) 71–79, https://doi.org/10.1016/0010-2180(81)90111-5.

[38] J.P. Hodges, S. Short, J.D. Jorgensen, X. Xiong, B. Dabrowski, S.M. Mini, C.W. Kimball, Evolution of oxygen-vacancy ordered crystal structures in the perovskite series $Sr_nFe_nO_{3n-1}$ (n= 2, 4, 8, and ∞), and the relationship to electronic and magnetic properties, J. Solid State Chem. 151 (2000) 190–209, https://doi.org/10.1006/jssc.1999.8640.

[39] G. Xiao, Q. Liu, S. Wang, V.G. Komvokis, M.D. Amiridis, A. Heyden, S. Ma, F. Chen, Synthesis and characterization of Mo-doped $SrFeO_{3-\delta}$ as cathode materials for solid oxide fuel cells, J. Power Sources 202 (2012) 63–69, https://doi.org/10.1016/j.jpowsour.2011.11.02.

[40] N.A. Baharuddin, A. Muchtar, M.R. Somalu, N.S. Kalib, N.F. Raduwan, Synthesis and characterization of cobalt-free $SrFe_{0.8}Ti_{0.2}O_{3-\delta}$ cathode powders synthesized through combustion method for solid oxide fuel cells, Int. J. Hydrogen Energy 44 (2019) 30682–30691, https://doi.org/10.1016/j.ijhydene.2018.11.142.

[41] J. Gao, Q. Li, Z. Zhang, Z. Lü, B. Wei, A cobalt-free bismuth ferrite-based cathode for intermediate temperature solid oxide fuel cells, Electrochem. Commun. 125 (2021) 106978, https://doi.org/10.1016/j.elecom.2021.106978.

[42] D. Muñoz-Gil, M.T. Azcondo, C. Ritter, O. Fabelo, D. Pérez-Coll, G.C. Mather, U. Amador, K. Boulahya, The effects of Sr content on the performance of $Nd_{1-x}Sr_xCoO_{3-\delta}$ air electrode materials for intermediate temperature solid oxide fuel cells under operational conditions, Inorg. Chem. 59 (17) (2020) 12111–12121, https://doi.org/10.1021/acs.inorgchem.0c01049.

[43] V. Cascos, L. Troncoso, J.A. Alonso, New families of M^{n+}-doped $SrCo_{1-x}M_xO_{3-\delta}$ perovskites performing as cathodes in solid-oxide fuel cells, Int. J. Hydrogen Energy 40 (2015) 11333–11341, https://doi.org/10.1016/j.ijhydene.2015.03.134.

[44] J. Wang, T. Yang, L. Lei, K. Huang, Ta-Doped $SrCoO_{3-\delta}$ as a promising bifunctional oxygen electrode for reversible solid oxide fuel cells: a focused study on stability, J. Mater. Chem. A 5 (2017) 8989–9002, https://doi.org/10.1039/C7TA02003.

[45] M.T. Fernández-Díaz, J.A. Alonso, Structural and electrical characterization of the novel $SrCo_{1-x}Ti_xO_{3-\delta}$ (x = 0.05, 0.1 and 0.15) perovskites: evaluation as cathode materials in solid oxide fuel cells, Renew. Energy 133 (2019) 205–215, https://doi.org/10.1016/j.renene.2018.09.073.

[46] A. Aguadero, D. Pérez-Coll, J.A. Alonso, S.J. Skinner, J. Kilner, A new family of Mo-doped $SrCoO_{3-\delta}$ perovskites for application in reversible solid state electrochemical cells, Chem. Mater. 24 (2012) 2655–2663, https://doi.org/10.1021/cm300255r.

[47] N.H. Perry, T. Ishihara, Roles of bulk and surface chemistry in the oxygen exchange kinetics and related properties of mixed conducting perovskite oxide electrodes, Materials 9 (2016) 858, https://doi.org/10.3390/ma9100858.

[48] R. Merkle, J. Maier, H.J.M. Bouwmeester, A linear free energy relationship for gas- solid interactions: correlation between surface rate constant and diffusion coefficient of oxygen tracer exchange for electron-rich perovskites, Angew. Chem. Int. Ed. 43 (2004) 5069–5073, https://doi.org/10.1002/anie.200460081.

[49] L. dos Santos-Gómez, J. Hurtado, J.M. Porras-Vázquez, E.R. Losilla, D. Marrero-López, Durability and performance of CGO barriers and LSCF cathode

deposited by spray-pyrolysis, J. Eur. Ceram. Soc. 38 (2018) 3518–3526, https://doi.org/10.1016/j.jeurceramsoc.2018.03.024.
[50] L. dos Santos-Gómez, J.M. Porras-Vázquez, E.R. Losilla, D. Marrero-López, Improving the efficiency of layered perovskite cathodes by microstructural optimization, J. Mater. Chem. A 5 (2017) 7896–7904, https://doi.org/10.1039/C6TA10946B.
[51] S.R. Bishop, D. Marrocchelli, C. Chatzichristodoulou, N.H. Perry, M.B. Mogensen, H.L. Tuller, E.D. Wachsman, Chemical expansion: implications for electrochemical energy storage and conversion devices, Annu. Rev. Mater. Res. 44 (2014) 205–239, https://doi.org/10.1146/annurev-matsci-070813-113329.